Computational Nanomechanics of Noncollagenous Interfibrillar Interface in Bone

Yang Wang, Reza Morsali, Zhengwei Dai, Majid Minary-Jolandan, and Dong Qian*

Cite This: *ACS Appl. Mater. Interfaces* 2020, 12, 25363−25373

[Read Online]

ACCESS | Metrics & More | Article Recommendations | Supporting Information

ABSTRACT: The noncollagenous interfibrillar interface in bone provides the critical function of transferring loads among collagen fibrils and their bundles, with adhesive mechanisms at this site thus significantly contributing to the mechanical properties of bone. Motivated by the experimental observations and hypotheses, a computational study is presented to elucidate the critical roles of two major proteins at the nanoscale interfibrillar interface, that is, osteopontin (OPN) and osteocalcin (OC) in bone. This study reveals the extremely high interfacial toughness of the OPN/OC composite. The previously proposed hypothesis of sacrificial bonds in the extracellular organic matrix is tested, and the remarkable mechanical properties of the nanoscale bone interface are attributed to the collaborative interactions between the OPN and OC proteins.

KEYWORDS: *bone, noncollagenous interfibrillar interface, interfacial shear toughness, osteopontin, osteocalcin, sacrificial bond*
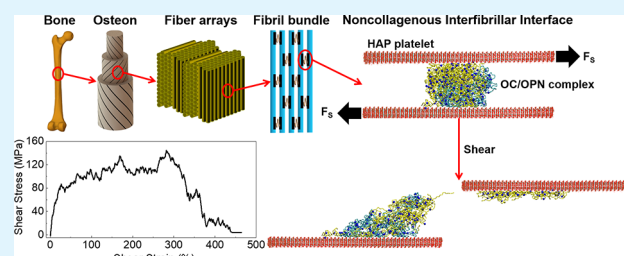
1. INTRODUCTION

Bone is a composite material made of fundamental constituents such as minerals, collagen, noncollagenous proteins, proteoglycans, and water, which are assembled in a fractal-like hierarchical fashion.[1−6] A hierarchical organization of bone with major components at each length scale is shown in Figure 1A.[6] At the molecular scale, tropocollagen molecules self-assemble into supertwisted collagen microfibrils through hydrogen bonding and covalent cross-linking[7,8] and are impregnated with hydroxyapatite (HAP) nanocrystals through biomineralization.[9] A recent experimental study demonstrated the 3D nanoscale organization of mineral in bone as part of its hierarchical assembly, where the mineral started as needle-shaped units that merged laterally to form platelets and further organized into stacks of platelets.[6]

Unlike conventionally engineered materials, healthy bone is known to be simultaneously stiff, strong, and fracture resistant. It has been shown that key mechanical properties such as stiffness and strength, and their degradation, are intimately linked to the mineral density,[10] microscopic architecture,[11] and microdamage.[12,13] Because mineral and protein on their own are either too brittle or too soft, the high fracture toughness in bone suggests strong synergistic effects enabled by interfaces across multiple length scales.

Significant progress has been made in understanding how bone interfaces at specific length scales contribute to fracture resistance. Both extrinsic (shield) and intrinsic (plasticity) toughening mechanisms[14] have been identified. The extrinsic toughening mechanisms act primarily at the microscale. Cement lines are the major microscale interfaces between

the osteon and bone matrix[15] and provide toughening mechanisms by crack deflection/twist and crack bridging.[14,16] Plasticity from the intrinsic toughening mechanisms takes place mainly at the submicrometer length scale. Specific deformation mechanisms include uncoiling of the tropocollagen, sliding within the mineralized collagen fibrils, and sliding between the collagen fibrils as part of collagen fiber.[14] Each collagen fiber contains multiple collagen fibrils that are twisted and bound together by a thin layer of the interfibrillar interface (Figure 1B, also referred to as the interfibrillar compartment, matrix, or space). When collagen is subjected to loads such as tension or bending, sliding between the neighboring fibrils takes place within the fiber as a result of the load transfer and leads to shear deformation of the interfibrillar interface. As discussed next, while several hypotheses have been proposed, a detailed understanding of the shear deformation mechanisms of the interfibrillar interface remains elusive.

The nanoscale interfibrillar interfaces occupy very small weight by percentage (~1%) in bone[17] and are mainly filled with noncollagenous proteins (NCPs). Major NCPs in the bone matrix include osteonectin (ON), fibronectin (FN), osteocalcin (OC), osteopontin (OPN), bone sialoprotein (BSP), and proteoglycans such as small leucine-rich
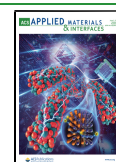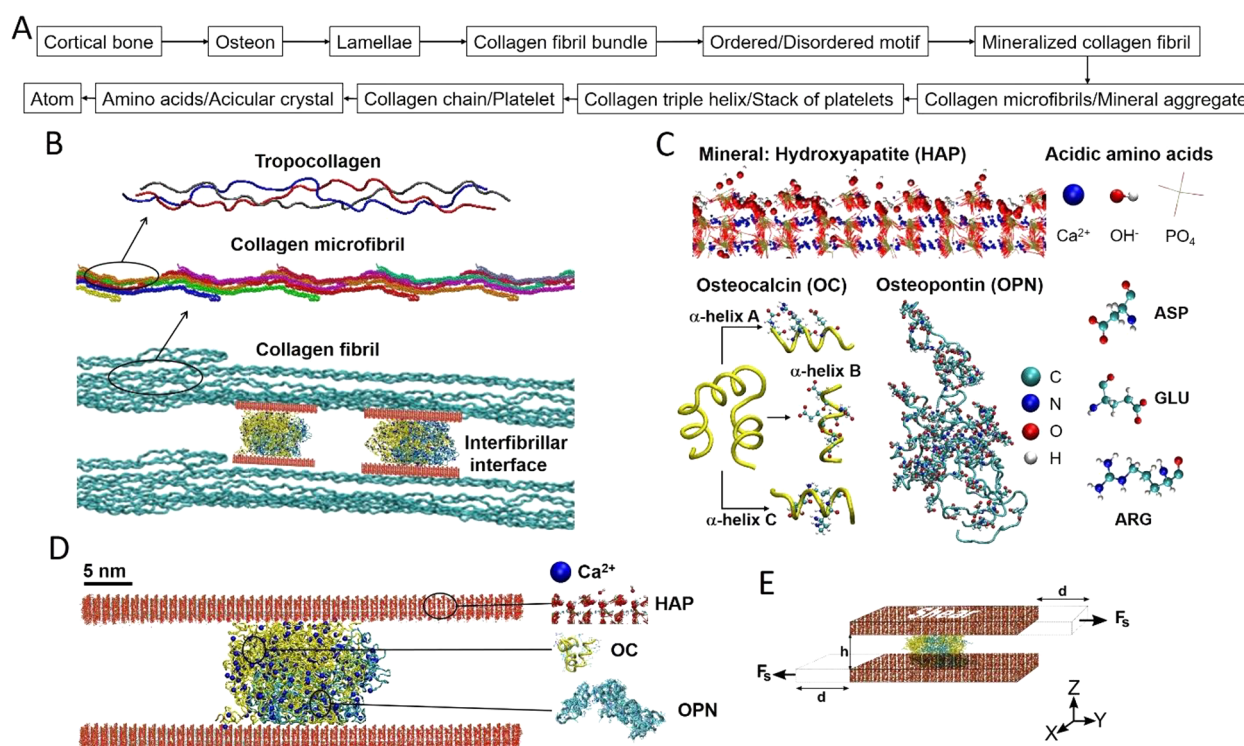
Figure 1. (A) Hierarchical organization of bone.[6] (B) The nanoscale interfibrillar interface: Each collagen fibril consists of collagen microfibrils that are assembled on the basis of tropocollagen.[44] (C) Structures of OC and OPN proteins and of HAP platelets. OC protein contains three α-helixes. OPN protein is an intrinsically disordered protein (IDP). Charged residues that serve as binding sites to anchor OC and OPN proteins to HAP are listed. (D) Configuration of the interface model before applying the shear load. OPN and OC proteins are colored in cyan and yellow, respectively. The composite model consists of two HAP platelets with dimensions of $32.1 \times 22.3 \times 2.4$ nm^3. (E) An illustration of the nanointerface model under shear.

proteoglycans (SLRPs) like decorin (DCN) and biglycan (BGN), etc.[18] Among these NCPs, OPN and OC proteins (Figure 1C) are abundant and closely linked to biomineralization[19−22] and bone remodeling.[23,24] OPN proteins interact either homotypically or heterotypically.[25] OPN acts similarly to an adhesive by binding strongly to both ionic and mineral lattice calcium atoms[26,27] and can repeatedly dissipate large amounts of energy by working against entropy.[28] The effectiveness of the OPN protein in its resistance to separation and energy dissipation can be further enhanced by Ca^{2+} ions[28,29] and additional cross-linking enabled by transglutaminase enzymes such as transglutaminase 2 (TG2) and Factor XIIIA.[26,30−32] OPN protein binds directly to OC,[33] which is known for its strong binding to bone minerals as well.[34] Because bone minerals can take the form of needles, platelets, and stacked platelets between the collagen fibrils,[4−6] we hypothesize that OC/OPN protein complexes at the interfibrillar interface contribute significantly to the intrinsic toughening mechanisms of bone.

Several mechanisms on the mechanics of the interfibrillar interface have been proposed on the basis of the experimental evidence. One suggested[29] that energy dissipation during separation of the collagen fibrils is accomplished through the "sacrificial bonds" within the interfibrillar interface and stretching of the molecular chains that are initially not loaded (also called the hidden length). The ability of this interface to accommodate large shear strain was demonstrated through an in situ tensile experiment of parallel-fibered bone.[35] On the other hand, formation of the "dilatational band" in noncollagenous protein complex of ~100 nm size for fatigue and

indentation tests of bone specimens was reported.[36,37] It was thus hypothesized that the dilatational band is mainly responsible for the nanoscale ductility and fracture toughness in bone. Further comparison with OC and/or OPN knockout mouse bone specimens confirmed the critical roles of OC/OPN proteins in regulating the band formation and fracture toughness. For instance, fracture toughness and work to fracture were observed to decrease significantly in OPN-deficient mice bones,[38,39] while lack of OC has been associated with reduced fracture load and stiffness.[40] A model of OC−OPN−OC in serial connection was proposed to provide the nanoscale deformation mechanisms responsible for the large energy dissipation.[41] In addition to the contributions from the OC/OPN proteins, it has also been suggested that direct contact between the HAP minerals and the collagen fibrils gave rise to friction and may provide an additional source of energy dissipation.[42,43]

In light of the significant challenges in experimentally probing the nanoscale interface and validating the proposed hypotheses, we established a computational model to quantify the role of noncollagenous OC/OPN protein complex in collagen interfibrillar interfacial load transfer. A molecular model of the collagen interfibrillar interface was constructed in the form of the composite of OC/OPN protein complex sandwiched between two HAP mineral platelets (Figure 1D and Figure S1). We postulated that the load transfer among the collagen fibrils was mainly realized through shear load transfer at the interface. Mechanical response and deformation mechanisms were subsequently investigated by applying simple shear load on the composite model (Figure 1E). Simulation
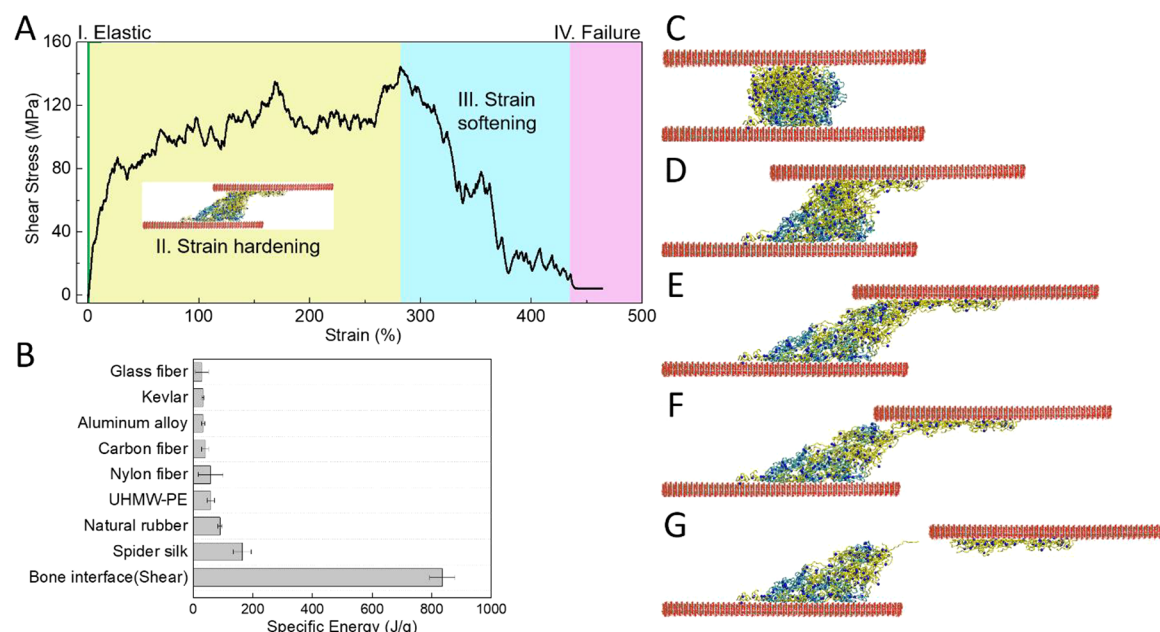
Figure 2. (A) Stress−strain response for the noncollagenous interfibrillar interface model under shear. Different background colors correspond to different stages of the stress−strain response: Green is the elastic region, yellow represents the strain hardening region, blue is for the strain softening, and pink is the failure region. (B) Specific energy comparison of the noncollagenous interfibrillar interface with other materials.[45−49] (C−G) Snapshots of the composite interface model under different shear strains. Calcium ions are plotted as dots. (C) At the elastic limit with 2.9% shear strain, the interface did not show visible shape change. (D) In the hardening region at 168.8% shear strain, the interface transformed into a parallelogram. (E) At the yielding point with 282.0% shear strain, localized deformation was observed near the top HAP platelet. (F) In the softening region with 354.7% shear strain, deformation was further localized, and the load was carried by a few OC proteins. (G) At the failure point with 435.4% shear strain, the interface split into two parts.

results revealed that the extremely high interfacial shear toughness was attributed to the synergistic effects of OC and OPN proteins.

The interfacial mechanical response was found to be contributed by both entropic conformational change and bond energy change. These findings provided the bases for a key molecular mechanism that is responsible for bone toughness. The specific energy to failure was 837.3 J/g, which is much higher than those of some of the well-known tough materials such as spider silk (165 J/g) and Kevlar (33 J/g).[45] The established computational model also provided important details on the mechanical response at the subnanometer scale. These results were employed to test the potential mechanisms that have been put forward on the basis of the experimental evidence.

2. RESULTS AND DISCUSSION

2.1. Stress−Strain Response. Figure 2A shows the shear stress−strain response of the interface, where four distinctive regions could be identified. The initial response was elastic. To evaluate the shear modulus, we first identified the elastic limit, which is defined as the stress below which the deformation is fully recoverable. For this purpose, the interface was loaded to different shear strain values and then fully unloaded to check if the applied strain can be fully recovered. These tests yielded a very narrow strain range of elastic response (2.9% shear strain) in the case of shear loading and the corresponding shear elastic limit of 16.0 MPa. By curve fitting of the linear portion of the elastic response, the shear modulus was obtained as 762.6 MPa (Figure S2).

The stress continued increasing after passing the elastic limit and entered into the second region of strain hardening. The

strain range for the hardening response was 279.1%. The shear stress−strain response demonstrated an interesting sawtooth pattern. The peak shear strength value was 144.4 MPa. Once the peak value was reached, the interface transitioned into the softening region. A similar sawtooth pattern of stress−strain relation was shown before the interface completely lost load-carrying capacity. The shear strain at failure was 435.4%.

The high strain range for the hardening and softening branches beyond the elastic limit is reflective of the ductile material behavior. To further quantify the ability of the interface to dissipate energy before failure, interfacial toughness was evaluated as the area under the stress−strain curve and the corresponding specific energy was 837.3 J/g. This value is much higher than those of most of the man-made or natural materials, as shown in Figure 2B. For instance, the toughness for shear is ∼5 times that for spider dragline silk, which has been known for its high toughness.[45] The high interfacial shear toughness is expected to contribute significantly to the bone toughness. The key mechanical properties are listed in Table 1.

2.2. Deformation Mechanism. Figure 2C−G provides snapshots of the OPN/OC interface model under shear strain values of 2.9%, 168.8%, 282.0%, 354.7%, and 435.4%, respectively. From Figure 2C, it can be seen that the

Table 1. Mechanical Properties for the Noncollagenous Interfibrillar Interface under Shear Load

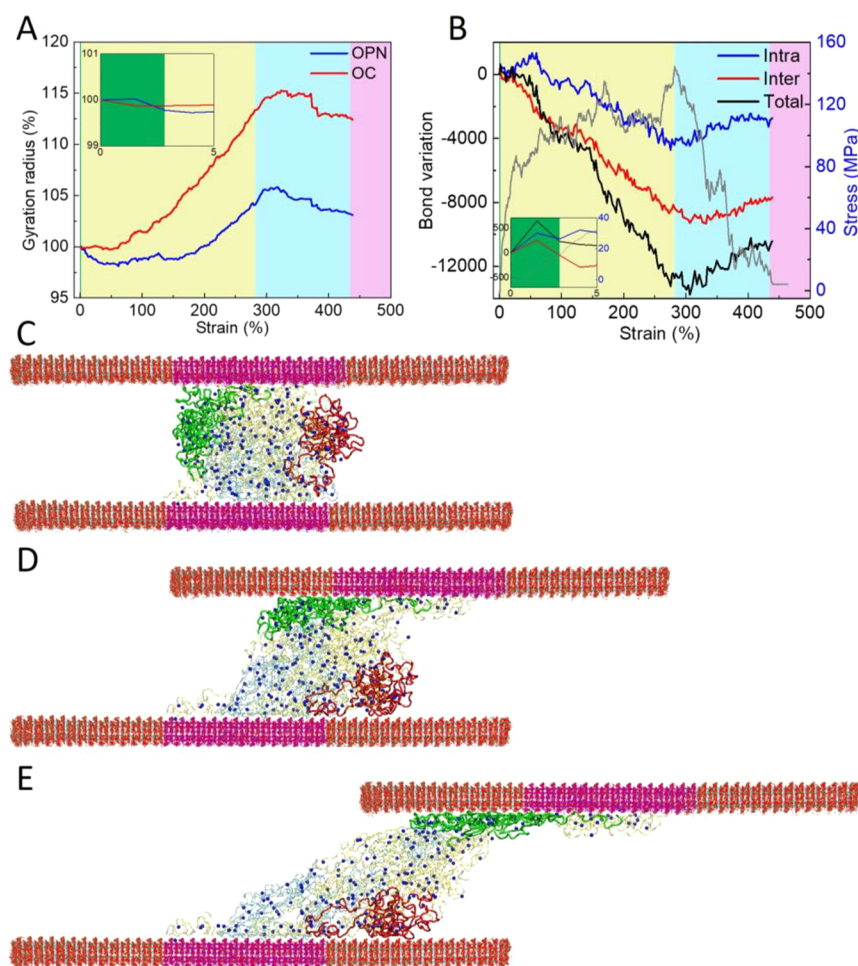|	modulus (MPa)	yield strength (MPa)	failure strength (MPa)	failure strain (%)	specific energy (J/g)
shear	762.6	144.4	13.2	435.4	837.3

Figure 3. (A) Evolution of the gyration radii R_g of the OPN and OC proteins under shear: the average R_g of the OC proteins and OPN proteins peaks at the shear strain of 323.2% and 317.7%, respectively. The inset shows the zoom-in view at the shear strain range of 0−5.0%. (B) Changes in the total number of nonbonded interactions: interchain interactions and intrachain interactions are plotted as functions of the shear strain. The inset shows the zoom-in view at the shear strain range of 0−5.0%. Shear stress−strain response is plotted in the background to demonstrate the correlation. (C−E) Snapshots of the interface at the shear strains of 0%, 130.0%, and 282.0%, respectively. One OPN and 22 OC proteins are colored in red and green, respectively, to illustrate the "rotate-and-crawl" motion.

composite roughly retained its shape within the elastic limit (up to the strain of 2.9%). To further quantify the deformation, gyration radii R_g values of the OPN and OC proteins were evaluated to provide measures on the mass distribution of each component around its center. In addition to R_g, the numbers of both nonbonded inter- and intrapolymer chain interactions within the composite were computed.

Elastic Response. The inset of Figure 3A shows the R_g of the OPN and OC proteins as functions of the strain up to the elastic limit. The applied shear load led to a minor change of 0.3% in R_g within this range. Similar trends were observed in the numbers of nonbonded inter- and intrapolymer chain interactions, as shown in the inset of Figure 3B, and the corresponding changes were 0.7% and 10.2%, respectively. These quantitative results indicated that OPN/OC composite underwent moderate deformation within the elastic limit and no significant configurational change of the chains has taken place.

Strain Hardening Response. Figure 2D and E shows the deformation pattern of the interface when it entered the strain hardening range (at 168.8% strain) and reached the peak shear strength (at 282.0% strain), respectively. The composite structure transformed into a skewed parallelogram shape to accommodate the shear load, which led to a general increase in the gyration radii in this strain range. For OC, R_g did not show a significant change up to the strain of 61.8%, after which it increased to 115.0% of its original value (Figure 3A). For OPN, a small reduction in R_g (∼2%) was observed between applied shear strains of 2.8% and 62.0%, followed by a moderate increase up to the strain of 192.0%. After this, R_g continued to increase, following a trend similar to that of OC, and reached 106.0% of its original value at the peak strength (Figure 3A).

The small reduction of R_g in the OPN proteins in the initial hardening stage (from 2.8% to 62.0% strain) was the direct result of the applied shear load. The interface maintained its original shape at this stage. The simple shear loading condition provided the principal tensile and compressive strain component at ∼45° and ∼135°, respectively, both with respect to the bottom HAP platelet. Subsequently, the tensile component resulted in the realignment of the chain as well as a reduction in the chain−chain distance. On the other hand, the compressive strain further reduced this distance and made part of OPN proteins that were aligned perpendicular to the compressive strain direction more compact. The reduction in the chain−chain distance led to enhanced intrachain
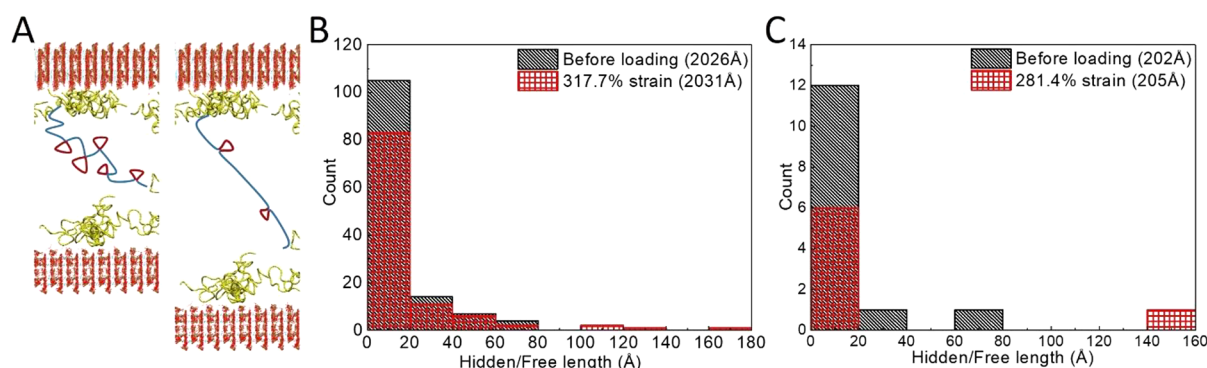
Figure 4. (A) An illustration of the sacrificial bond, free length (colored in blue), hidden length (colored in red), and the breaking of the sacrificial bonds converting hidden length to free length. (B) Segment length (including both hidden and free lengths) distributions of the OPN3 protein at the shear strain of 0% and 317.7%. (C) Segment length (including both hidden and free lengths) distributions of the OC19 molecule at the shear strain of 0% and 281.4%. Total lengths of the chains are shown in parentheses in (B) and (C).

interaction at this range, as shown in Figure 3B. In contrast, no significant reduction of the chain−chain distance was observed in the OC proteins for this range of strain, because OC proteins are short-chained molecules and were not directly influenced by the shear load.

The applied shear load also caused the proteins to roll over the HAP platelets, as shown in Figure 3C−E. As a result, some OPN and OC proteins (marked in Figure 3C−E) were observed to develop a "rotate-and-crawl" motion; that is, these proteins rotated from the center of the interface to create more contact with HAP. This resulted in additional anchoring points and binding sites between the proteins and HAP and further enhanced the load transfer from the HAP to the protein complex. The generation of these additional binding sites is unique to this biointerface and contributes significantly to both the ductile behavior and the high shear toughness. A detailed analysis of the OPN−HAP interaction showed that it was dominated by two types of nonbonded interactions: First, OPN protein binds to the HAP platelet surface through its ASP and GLU residues (Figure S3A and B). The ASP and GLU residues are negatively charged so that they directly interact with the calcium ions in HAP. Second, the hydrogen atoms in ARG of the OPN protein can form hydrogen bonds with oxygen atoms in hydroxide and phosphate in HAP (Figure S3C). Similarly, OC proteins have a rich content of ASP, GLU, and ARG residues and adhere to the HAP surface through the same types of electrostatic interactions with the calcium ions and the hydrogen bonds with oxygen atoms in HAP (Figure S3D and E). The benefits of the observed "rotate-and-crawl" mechanism can be quantified by the numbers of nonbonded OC−HAP and OPN−HAP inter-actions at the interface as shown in Figure S5A. It can be seen that these interactions consistently increased during the hardening stage. Furthermore, the values for the OC−HAP interaction were higher than those for the OPN−HAP interaction, indicating OC proteins were more active in anchoring the proteins to HAP.

Figure S5A also shows that the interchain interactions of OC−OC, OC−OPN, and OPN−OPN have all decreased in the strain hardening region. This reduction of interaction suggested that the protein complex was unraveling as the interface transitioned into the skewed shape after the shear strain of ~55.0% as shown in Figure 2D. More importantly, reduction in the OC−OC interaction was observed to be the most significant, which indicated the separations among the

OC proteins. Similar to the case of interacting with HAP, calcium ions contributed to the formation of the interchain interactions within the OC/OPN complex by acting as the bridge to link multiple negatively charged residues, ASP or GLU (Figure S4). As such, these interactions are electrostatic.

Figure S5B provides the same trend of loss in the intrachain interactions within the individual OC and OPN proteins that occurred concurrently with the interchain interactions. The overall effects on the nonbonded interactions of each protein component are shown in Figure S5C. These are indications of disentanglement in both the OC and the OPN proteins, which continued toward the later part of the hardening stage and were accompanied by large separations among the OC proteins and between the OPN and OC proteins. The disentanglement was accompanied by the continuing increase in R_g in both the OC and the OPN proteins, as shown in Figure 3A for the later part of the hardening stage (>62.0% shear strain).

Strain Softening Response. Figure 2F and G shows the deformation pattern of the interface corresponding to the softening region (354.7% strain) and the complete interface separation (435.4% strain). Some protein chains continued being stretched and unfolded as the softening response started. The unfolding event was demonstrated through the change in R_g as shown in Figure 3A. Specifically, the R_g values of both the OC and the OPN proteins first increased and then decreased in the softening region. This switch was due to the stretch in the protein chains followed by detachment from the opposite side that resulted in failure as shown in Figure 2G. Figure S5A shows that the change in the OC−OC interaction remained as the most significant contributor. The OC−HAP interaction maintained the increasing trend in this region, indicating that the rotate-and-crawl behavior continued after the yielding point to generate more binding sites.

2.3. Sacrificial Bond, Hidden Length, and Contributions to Stress−Strain Response. On the basis of the experiments,[29] an interesting hypothesis has been proposed on the links among the interfacial deformation, hidden length, free length, sacrificial bonds, and stress−strain response. Sacrificial bonds refer to the nonbonded interactions within the single protein chain itself (intrachain interactions). Their presence prevents segments within the protein chains from being directly subjected to loads (shown as small loops in Figure 4A). The corresponding lengths of the segments are termed hidden lengths as these segments do not carry the load before
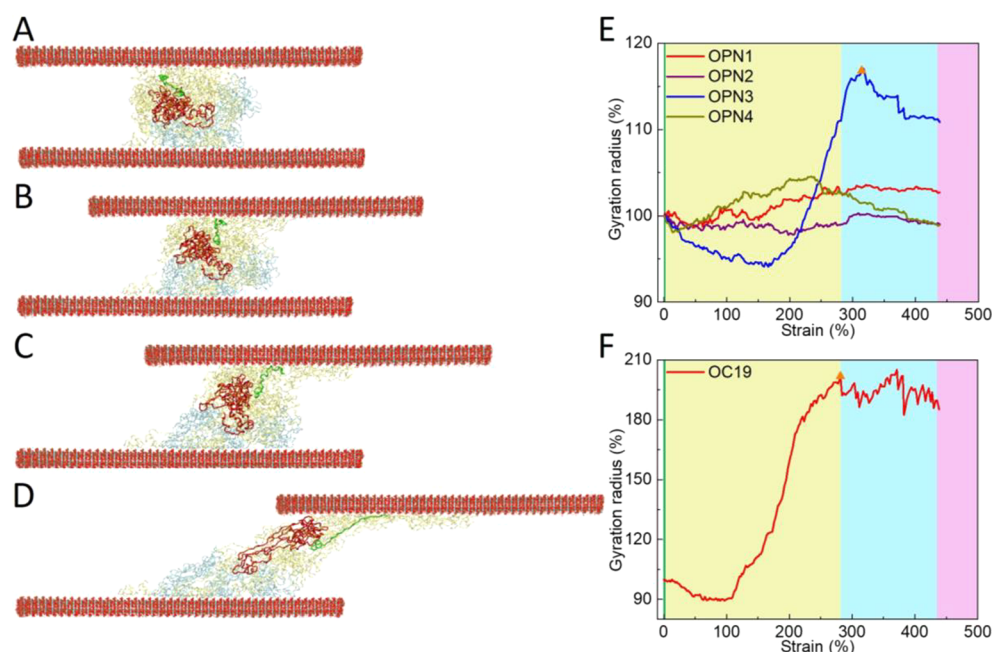
Figure 5. (A−D) Snapshots of the interface at 0%, 95.0%, 151.0%, and 314.0% shear strain, respectively. OPN3 and OC19 proteins are colored in red and green, respectively, to demonstrate the mechanism of the sacrificial bonds. (E) Evolution of the gyration radii for four OPN proteins as functions of the shear strain. (F) Evolution of the gyration radius for protein OC19 as functions of the shear strain. The orange triangles correspond to the peak points.

the sacrificial bonds are broken and thus provide the important mechanism of energy dissipation. In contrast, the lengths that correspond to the protein segments carrying the load are termed free lengths. When the sacrificial bonds break, a segment of the hidden length is activated and adds to the free length of the chain that transfers the load. It was proposed that the interfacial mechanical response is governed by the mechanism of sacrificial bonds and can be described by the entropic elasticity model.[50,51]

The great level of details revealed from the simulation enabled us to test the hypothesis on the mechanism of sacrificial bonds. In the current system, the sacrificial bonds correspond to the intrachain interactions within the OC and OPN proteins. To confirm the conversion from the hidden to free length through the sacrificial bond mechanism, distributions of the hidden and free lengths for two representative molecules, that is, OPN3 and OC19 proteins (as shown in Figure 5A−D), were monitored during the shear load. Figure 4B provides the distributions of the segment lengths for OPN3 before the application of the shear load and at the shear strain of 317.7%. The gyration radius of OPN3 peaked at this shear strain. The applied shear load led to a reduction in the number of chain segments (from 105 to 83) with initial lengths less than 20 Å. The merging of these short chains produced four long-chain segments with free lengths >100 Å. Figure 4C presents a similar trend in the change of chain segment length distribution for OC19 when its gyration radius peaked at the applied shear strain of 281.4%. The number of short-chain segments changed from 12 to 6 and resulted in a long chain with a length of 151 Å. In contrast with the significant changes in the segment lengths, the total lengths for both chains remained almost unchanged as shown in Figure 4B and C.

Figure 5E shows the trends in R_g for four OPN proteins in the system (marked as OPN1−OPN4). All experienced moderate changes except for protein OPN3. Figure 5F

provides the change in R_g as a function of the applied shear strain for one OC protein, marked as OC19. Snapshots of the deformed OPN3 and OC19 proteins are shown in Figure 5A− D. It can be seen that the applied shear load led to significant deformation in both molecules in the later part of the hardening. As a result, both molecules got stretched, and more straightened segments (free lengths) were generated (Figure 5D) and aligned with the stretch to resist the load. These additions contributed to the sawtooth pattern in the stress− strain curve with multiple peaks (Figure 2A). It also explained the rapid increase in R_g in Figure 5E and F. Because the mechanism of sacrificial bond prevented the entire chains of the OC and OPN proteins from being loaded at once, it contributed to both the high ductility and the high toughness as observed in the simulation.

Detailed analysis of the evolution of molecular structure revealed two major types of sacrificial bonds. The first was due to the nonbonded interactions within the OC and OPN proteins, referred to as the intrachain interaction as shown in Figure 6A−F. All of the interactions are electrostatic and require calcium ions to serve as the bridges. The second type of sacrificial bonds, which was not discussed before,[50] was due to the interchain interactions between the OC and OPN proteins or between two OC or OPN proteins. Examples of such kind of interactions are shown in Figure S4. Like the first type, it is also electrostatic and mediated by calcium ions. Breakage of the second type of sacrificial bonds does not necessarily convert the hidden length to free length; however, it does reduce the entropy of the system by merging short segments into long ones (Figure S4D).

In addition to the sacrificial bonds, changes of the energy due to nonbonded interactions between the protein chains (interchain) were also evaluated and compared to the intrachain interactions as shown in Figure 7A. Change in interchain interactions among the OC proteins provided the
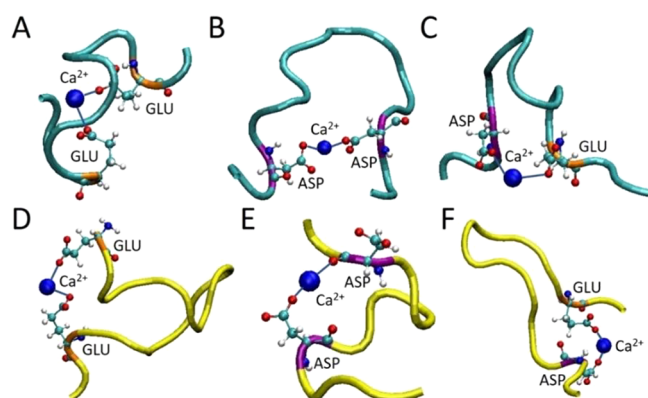
Figure 6. Sacrificial bonds due to intrachain interactions within the OPN protein (A–C) and OC protein (D–F). All interactions are mediated by calcium ions.

most significant contribution, which is higher than the sacrificial bonds within either the OC or the OPN proteins (change in intrachain interactions). Furthermore, nonbonded interaction energy changes within the OPN proteins (both inter- and intrachain) are comparable to but generally less than those within the OC proteins, indicating the OPN proteins were less active. Figure 7A also shows that the interchain interaction between the OC and OPN proteins was the second most important contributor to the overall nonbonded interactions toward the late stage of the strain hardening region (>160.0% shear strain) as well as in the region of strain softening. These observations suggest that the OPN and OC proteins work collaboratively to provide high ductility and toughness. The detailed mechanism of the collaborative effects is discussed in the following section. A notable change of trend was observed in the nonbonded interactions between the OPN and OC proteins, which was caused by the fact that much of the protein complex was detached from the opposite side and bounced back to recover the relaxed shape (Figure 2F).

In addition to nonbonded interactions, changes in the energies of bonded interactions as functions of the shear strain were also evaluated and shown in Figure 7B. The total bonded energy change was observed to be comparable to the nonbonded energy change up to ~175.0% shear strain, after which the two deviated with the bonding energy change being lower (Figure 7C). The large difference between the two was observed in the softening region, which was caused by the

detachment of the OC/OPN complex from the opposite side. This led to the relaxation of the OC/OPN proteins, and the bonding energy decreased while the nonbonded energy was less affected. The maximum difference between the two was 69.5%. The intrachain interaction (sacrificial bond) was responsible for ~32.0% of the nonbonded interactions for most of the shear strain values applied (Figure 7C). These comparisons lead to the conclusion that the interface shear response is not entirely entropic because the energy costs for bond deformation and nonbonded interaction (including the sacrificial bond) were of the same order. More importantly, energy associated with the sacrificial bonds was significant but not dominant. Figure 7B shows that the bonding energy change in the OC proteins was about 145.0% of the corresponding in the OPN proteins for the range of applied shear strain. A further breakdown of the bonding energy into contributions from the bond stretch, bending, and twist is shown in Figure S6. It can be concluded that the conformational change of the OC/OPN complex is accompanied by significant changes in bond length, bond angle, and dihedral angle. These changes are expected as the shear load tends to stretch the individual protein chain to transform it into either a fully or a partially straight shape. The contribution from the bond angle (bending term) was the most significant.

2.4. Collaborative Roles of the OC and OPN Proteins. To further elucidate the combined roles of the OC and OPN proteins in the composite model, we also conducted the simulations on the interface involving only the OC or OPN proteins, respectively. The OC-only and OPN-only models were obtained by removing the other component in the original composite model and then thermodynamically equilibrating the single-component system before applying the shear load. A comparison of the shear force–displacement responses is shown in Figure 8A. This comparison demonstrated that the composite model provided the best mechanical performance. More specifically, peak force and energy dissipation in the composite system were the highest among the three models. A combination of the OC and OPN proteins enabled the interface to achieve higher shear stiffness (762.6 MPa) and dissipate more energy (537.6 aJ) than the interface with a single component. Although the OPN-only interface model provided the highest ductility, the peak force it accomplished was only 30.4% of the composite system. Quantitative comparisons on the key mechanical properties
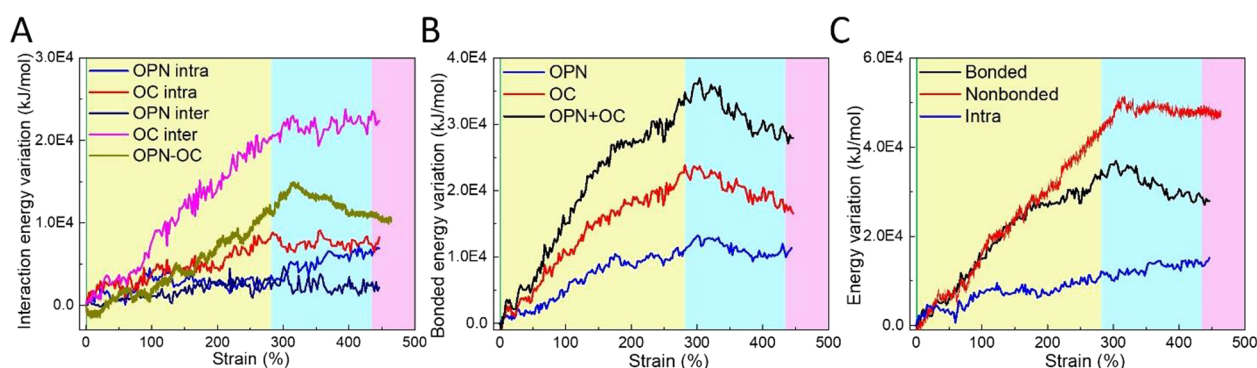

Figure 7. (A) Changes in the nonbonded interaction energies as functions of the applied shear strain. The energy terms include the intrachain interaction within the OPN and OC proteins, the interchain interaction within the OPN proteins or OC proteins, and the interchain interaction between the OPN and OC proteins. (B) Changes in bonded energy in the OPN and OC proteins and the sum of the two as functions of the shear strain. (C) Comparison among the bonded, nonbonded energies, and nonbonded energy due to intrachain interactions (sacrificial bond).
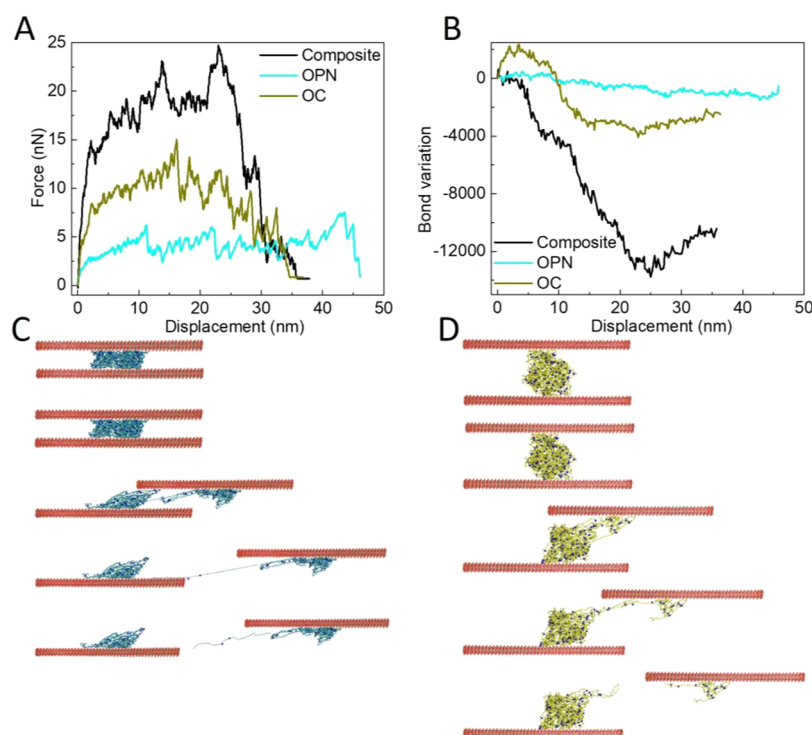
Figure 8. (A) Comparison of the shear force−displacement responses among the OPN/OC composite system and systems with only OPN proteins or OC proteins. (B) Changes in the numbers of nonbonded interactions in the interface proteins as functions of the shear displacement. (C) Snapshots of the OPN-only system under the shear load. The corresponding shear displacement values are 0, 0.2, 21.7, 43.5, and 44.7 nm from top to bottom. (D) Snapshots of the OC-only system under the shear load. The corresponding shear displacement values are 0, 0.4, 16.2, 27.5, and 34.2 nm from top to bottom.

are shown in Table 2. It is worth noting that the interfacial shear toughness values of the OC-only and OPN-only system were 56.6% and 35.7% of the corresponding composite system.

Table 2. Comparison of the Mechanical Properties for the OC/OPN/Composite Model

	mechanical properties under shear		
	modulus (MPa)	ultimate force (nN)	energy dissipation (aJ)
composite	762.6	24.7	537.6
OPN	329.4	7.5	192.0
OC	814.4	15.0	304.4

Deformation patterns of the OPN-only and OC-only interfaces under the applied shear load are shown in Figure 8C and D, respectively. The response from the OPN-only system was observed to be highly compliant. A single chain emerged in the strain hardening stage as the main component to take up the shear load, which was stretched to 232.8% of its original gyration radius. The conformational state change did not involve significant breakage of the sacrificial bonds. The observed good ductility of the interface was attributed to two factors: First, stiffness of the long-chain unstructured OPN proteins was lower than the OPN/OC composite, as evidenced by the load−displacement curve shown in Figure 8A. Second, part of the OPN proteins was seen to slide on the HAP surface (Figure 8C) before they were completely detached. As such, peak force was low due to the weak bonding between the OPN proteins and HAP that led to the detachment instead of the breakage of the chain backbone (Figure 8C). In contrast, the OC-only system demonstrated stiffer behavior. It first rotated

under the shear load, which led to more binding sites between the OC proteins and HAP. As a result, interfacial failure of the OC-only system was in the form of chain−chain separation within the OC proteins (Figure 8D) rather than the detachment from the HAP as in the case of OPN-only interface. This key difference was responsible for the higher peak force in the composite system than that in the OPN-only system. Although comparable ductility has been demonstrated, energy dissipation in the OC-only system was much lower than that in the composite system due to the short-chain nature of the OC protein that provided much less sacrificial bonds.

The above-described collaborative effects between the OPN and OC proteins and comparison with the single-component systems were further quantified. As evidenced by the change in the nonbonded interactions shown in Figure 8B, the applied shear load led to the loss of inter- and intrachain interactions in all three models. However, changes in the OPN- and OC-only systems were far less significant. These comparisons accounted for the differences in both the interfacial shear toughness and the peak shear force. Figure S7 shows that the interaction with HAP was significantly reduced when OC and OPN proteins were not present simultaneously in the model, which was supported by the earlier observation of the lack of rotate-and-crawl behavior of proteins in the deformation patterns shown in Figure 8C and D.

3. CONCLUSIONS

Motivated by recent experiments on the nanoscale bone interface, new insights on the mechanisms of the interfibrillar interface have been presented. On the basis of a composite model featuring the combination of noncollagenous proteins of OC and OPN, computational studies revealed extremely the

high shear toughness (837.3 J/g) of the nanoscale bone interface. The unique ability of the interface to accomplish high energy dissipation while maintaining good ductility was attributed to the collaborative roles of the OC and OPN proteins. More specifically, both bonded and nonbonded interactions within the OC proteins provided the largest contribution to the interfacial shear toughness. Furthermore, OC proteins facilitated the binding between the protein complex and the HAP platelets by tightly anchoring the ends of the OPN proteins to HAP. This effectively prevented the detachment at the interface and led to high ductility and energy dissipation through the unfolding of the OC and OPN proteins. The high ductility was also attributed to the stretch of the long chains of OPN proteins that assumed the bundled form in the initial configuration. Additionally, dynamic binding sites were found to form between the OPN and OC proteins, and this kind of dynamic bond can reform during the load process due to the highly compliant nature of the OPN protein. While the sacrificial bond played an important role in the interfacial mechanical response, contribution from the interchain interaction and deformation of the bond (stretch, bending, dihedral) were also significant. On the basis of these observations, it is concluded that the overall response of the interface was driven by changes in both the entropy associated with the conformational change of the interface and the internal energy.

The important advantage of the synergistic effects between OC and OPN proteins was further validated through an analysis of the single-component system involving either the OC or the OPN proteins, respectively. The computational results thus tested the hypothesis that was put forward before.[50,52] Although dilatational band formation was not observed in the simulation as reported in the experiment,[36] we postulated that its formation has an intrinsic length scale that is beyond the scope of the currently employed atomistic simulation. For example, sizes of the experimentally observed dilatation bands are typically on the order of 0.5−1 μm.[36] These experimental observations did suggest, however, a potential link between the deformation mechanisms at the nano and micrometer scales. Fully capturing this critical link will require multiscale computational techniques. Finally, it should be noted that this study does not exclude the potential roles of other NCPs, such as SLRPs, in contributing to the mechanical properties of the interfibrillar interface. While the focus of this study is on bone, the interfibrillar interfaces in ligaments and tendons are different. For instance, in tendon the proteins comprising the interfibrillar matrix are mainly the SLRPs.[53] Further investigations are needed to understand the mechanisms of these interfibrillar interfaces and the roles of SLRP and other NCPs.

4. MATERIALS AND METHODS

Atomistic Models of OC, OPN, and HAP. Configuration of the OC protein was obtained from the protein data bank website (PID: 1VZM).[54,55] The initial random structural model of the OPN protein was generated on the basis of the residue sequence obtained from the National Center for Biotechnology Information, U.S. National Library of Medicine (https://www.ncbi.nlm.nih.gov/). This structure was first equilibrated under 300 K for 20 ns. The equilibrated OPN protein was further placed in a water box of 25 × 25 × 25 nm^3 and equilibrated under 300 K for another 10 ns. The HAP platelet was generated on the basis of the HAP unit cell, which has 44 atoms and lattice parameters of a = 9.417 Å, b = 9.417 Å, c = 6.875 Å, α = 90°, β

= 90°, and γ = 120°.[56] The [001] surface of the HAP was utilized as the contact surface for the interface.

System Assembly and MD Simulation. The interface model consists of 4 OPN, 64 OC proteins, and 2 HAP platelets with each OC, OPN protein, and HAP platelet containing 493, 4741, and 89 056 atoms, respectively. Each of the two HAP platelets contains 2024 HAP unit cells and has identical dimensions of 32.1 × 22.3 × 2.4 nm.[57] The aforementioned numbers of OC, OPN proteins, and HAP dimensions were prescribed on the basis of experiments.[17,58] The OC and OPN proteins were initially positioned randomly within a 40 × 40 × 40 nm^3 box and then subjected to energy minimization with periodic boundary conditions. The system was then annealed using a NPT ensemble with a constant pressure of 1 atm, and the temperature was increased from 300 to 1200 K for 10 ns with a step size of 100 K. After this, the system pressure was increased from 1 to 6 atm for 6 ns with a step size of 1 atm. The system temperature then was reduced to 300 K and maintained for 1 ns, followed by the reduction of the pressure to 1 atm for another 4 ns while keeping the temperature at 300 K. The protein system was further neutralized with 220 Ca^{2+} ions and placed between the two HAP platelets by aligning the mass center of the proteins with the two HAP platelets. After another round of energy minimization, the system was compressed by applying a constant force of 10 000 kJ/mol/nm to generate initial binding sites between the HAP platelets and the proteins. The force was then released after the equilibration. The final equilibration process was conducted before the application of shear load. Shear deformation was introduced by applying a pulling velocity of 0.002 nm/ps to the top and bottom HAP platelets in opposite directions using steered molecular dynamics (SMD). All simulations were carried out using the MD simulation package GROMACS with the charmm36 force field.[43]

Analysis of Simulation Results. Shear stress and strain were defined as $\tau = F_s/A_0$ and $\gamma = \delta_s/h$, respectively. Here, F_s is the applied shear force, A_0 is the initial in-plane area of the proteins, δ_s is the displacement of the top HAP platelet with respect to the bottom HAP platelet in the tangential direction, and h is the initial net distance between the two HAP platelets as shown in Figure 1E. The specific energy was evaluated by dividing the area under the shear stress−strain curve by the mass density of the interface. The mass density is given as the mass of the interface divided by the volume. The mass of the interface includes the OC and OPN proteins as well as the ions. The volume of the interface is given as the product of the area A_0 and distance h.

■ ASSOCIATED CONTENT

Ⓢ Supporting Information

The Supporting Information is available free of charge at https://pubs.acs.org/doi/10.1021/acsami.0c01613.

> Model geometry, binding sites, gyration radius, sacrificial bond, hidden length, free length, and bonded and nonbonded interaction energies (PDF)

■ AUTHOR INFORMATION

Corresponding Author

Dong Qian — *Department of Mechanical Engineering, The University of Texas at Dallas, Richardson, Texas 75080, United States;* ⓞ orcid.org/0000-0001-9367-0924; Email: dong.qian@utdallas.edu

Authors

Yang Wang — *Department of Mechanical Engineering, The University of Texas at Dallas, Richardson, Texas 75080, United States*

Reza Morsali — *Department of Mechanical Engineering, The University of Texas at Dallas, Richardson, Texas 75080, United States*

Zhengwei Dai − *College of Material and Textile Engineering, Jiaxing University, Jiaxing 314001, People's Republic of China*

Majid Minary-Jolandan − *Department of Mechanical Engineering, The University of Texas at Dallas, Richardson, Texas 75080, United States;* ⊙ orcid.org/0000-0003-2472-302X

Complete contact information is available at:
https://pubs.acs.org/10.1021/acsami.0c01613

Notes
The authors declare no competing financial interest.

■ REFERENCES

(1) Weiner, S.; Wagner, H. D. The material bone: structure-mechanical function relations. *Annu. Rev. Mater. Sci.* **1998**, *28* (1), 271−298.

(2) Rho, J.-Y.; Kuhn-Spearing, L.; Zioupos, P. Mechanical properties and the hierarchical structure of bone. *Med. Eng. Phys.* **1998**, *20* (2), 92−102.

(3) Hamed, E.; Lee, Y.; Jasiuk, I. Multiscale modeling of elastic properties of cortical bone. *Acta Mech.* **2010**, *213* (1−2), 131−154.

(4) Reznikov, N.; Shahar, R.; Weiner, S. Bone hierarchical structure in three dimensions. *Acta Biomater.* **2014**, *10* (9), 3815−3826.

(5) Reznikov, N.; Shahar, R.; Weiner, S. Three-dimensional structure of human lamellar bone: The presence of two different materials and new insights into the hierarchical organization. *Bone* **2014**, *59*, 93−104.

(6) Reznikov, N.; Bilton, M.; Lari, L.; Stevens, M. M.; Kröger, R. Fractal-like hierarchical organization of bone begins at the nanoscale. *Science* **2018**, *360* (6388), No. eaao2189.

(7) Perumal, S.; Antipova, O.; Orgel, J. P. R. O. Collagen fibril architecture, domain organization, and triple-helical conformation govern its proteolysis. *Proc. Natl. Acad. Sci. U. S. A.* **2008**, *105* (8), 2824−2829.

(8) Orgel, J. P. R. O.; Irving, T. C.; Miller, A.; Wess, T. J. Microfibrillar structure of type I collagen in situ. *Proc. Natl. Acad. Sci. U. S. A.* **2006**, *103*, 9001−9005.

(9) Ma, J.; Wang, J.; Ai, X.; Zhang, S. Biomimetic self-assembly of apatite hybrid materials: From a single molecular template to bi-/multi-molecular templates. *Biotechnol. Adv.* **2014**, *32* (4), 744−760.

(10) Ciarelli, M. J.; Goldstein, S. A.; Kuhn, J. L.; Cody, D. D.; Brown, M. B. Evaluation of orthogonal mechanical properties and density of human trabecular bone from the major metaphyseal regions with materials testing and computed tomography. *J. Orthop. Res.* **1991**, *9* (5), 674−682.

(11) Müller, R. The Zürich Experience: One Decade of Three-Dimensional High-Resolution Computed Tomography. *Top. Magn. Reson. Imaging* **2002**, *13* (5), 307−322.

(12) Reilly, G. C.; Currey, J. D. The effects of damage and microcracking on the impact strength of bone. *J. Biomech.* **2000**, *33* (3), 337−343.

(13) Burr, D. B.; Turner, C. H.; Naick, P.; Forwood, M. R.; Ambrosius, W.; Sayeed Hasan, M.; Pidaparti, R. Does microdamage accumulation affect the mechanical properties of bone? *J. Biomech.* **1998**, *31* (4), 337−345.

(14) Launey, M. E.; Buehler, M. J.; Ritchie, R. O. On the Mechanistic Origins of Toughness in Bone. *Annu. Rev. Mater. Res.* **2010**, *40* (1), 25−53.

(15) Burr, D. B.; Schaffler, M. B.; Frederickson, R. G. Composition of the cement line and its possible mechanical role as a local interface in human compact bone. *J. Biomech.* **1988**, *21* (11), 939−945.

(16) Koester, K. J.; Ager, J. W.; Ritchie, R. O. The true toughness of human cortical bone measured with realistically short cracks. *Nat. Mater.* **2008**, *7* (8), 672−677.

(17) Barthelat, F.; Yin, Z.; Buehler, M. J. Structure and mechanics of interfaces in biological materials. *Nat. Rev. Mater.* **2016**, *1* (4), 16007.

(18) Gehron Robey, P. Chapter 17 - Noncollagenous Bone Matrix Proteins. In *Principles of Bone Biology*, 3rd ed.; Bilezikian, J. P., Raisz, L. G., Martin, T. J., Eds.; Academic Press: New York, 2008; pp 335−349.

(19) Addison, W. N.; Masica, D. L.; Gray, J. J.; McKee, M. D. Phosphorylation-dependent inhibition of mineralization by osteopontin ASARM peptides is regulated by PHEX cleavage. *J. Bone Miner. Res.* **2009**, *25* (4), 695−705.

(20) Azzopardi, P. V.; O'Young, J.; Lajoie, G.; Karttunen, M.; Goldberg, H. A.; Hunter, G. K. Roles of Electrostatics and Conformation in Protein-Crystal Interactions. *PLoS One* **2010**, *5* (2), No. e9330.

(21) Boskey, A. L.; Christensen, B.; Taleb, H.; Sørensen, E. S. Post-translational modification of osteopontin: Effects on in vitro hydroxyapatite formation and growth. *Biochem. Biophys. Res. Commun.* **2012**, *419* (2), 333−338.

(22) Chen, L.; Jacquet, R.; Lowder, E.; Landis, W. J. Refinement of collagen−mineral interaction: A possible role for osteocalcin in apatite crystal nucleation, growth and development. *Bone* **2015**, *71*, 7−16.

(23) Sodek, J.; Ganss, B.; McKee, M. D. Osteopontin. *Crit. Rev. Oral Biol. Med.* **2000**, *11* (3), 279−303.

(24) Lee, N. K.; Sowa, H.; Hinoi, E.; Ferron, M.; Ahn, J. D.; Confavreux, C.; Dacquin, R.; Mee, P. J.; McKee, M. D.; Jung, D. Y.; Zhang, Z.; Kim, J. K.; Mauvais-Jarvis, F.; Ducy, P.; Karsenty, G. Endocrine regulation of energy metabolism by the skeleton. *Cell* **2007**, *130* (3), 456−469.

(25) Goldsmith, H. L.; Labrosse, J. M.; McIntosh, F. A.; Mäenpää, P. H.; Kaartinen, M. T.; McKee, M. D. Homotypic Interactions of Soluble and Immobilized Osteopontin. *Ann. Biomed. Eng.* **2002**, *30* (6), 840−850.

(26) Cavelier, S.; Dastjerdi, A. K.; McKee, M. D.; Barthelat, F. Bone toughness at the molecular scale: A model for fracture toughness using crosslinked osteopontin on synthetic and biogenic mineral substrates. *Bone* **2018**, *110*, 304−311.

(27) McKee, M. D.; Pedraza, C. E.; Kaartinen, M. T. Osteopontin and Wound Healing in Bone. *Cells Tissues Organs* **2011**, *194* (2−4), 313−319.

(28) Fantner, G. E.; Adams, J.; Turner, P.; Thurner, P. J.; Fisher, L. W.; Hansma, P. K. Nanoscale Ion Mediated Networks in Bone: Osteopontin Can Repeatedly Dissipate Large Amounts of Energy. *Nano Lett.* **2007**, *7* (8), 2491−2498.

(29) Fantner, G. E.; Hassenkam, T.; Kindt, J. H.; Weaver, J. C.; Birkedal, H.; Pechenik, L.; Cutroni, J. A.; Cidade, G. A. G.; Stucky, G. D.; Morse, D. E.; Hansma, P. K. Sacrificial bonds and hidden length dissipate energy as mineralized fibrils separate during bone fracture. *Nat. Mater.* **2005**, *4* (8), 612−616.

(30) Kaartinen, M. T.; Murshed, M.; Karsenty, G.; McKee, M. D. Osteopontin upregulation and polymerization by transglutaminase 2 in calcified arteries of Matrix Gla protein-deficient mice. *J. Histochem. Cytochem.* **2007**, *55* (4), 375−386.

(31) Forsprecher, J.; Wang, Z.; Goldberg, H. A.; Kaartinen, M. T. Transglutaminase-mediated oligomerization promotes osteoblast adhesive properties of osteopontin and bone sialoprotein. *Cell Adhes. Migr.* **2011**, *5* (1), 65−72.

(32) Christensen, B.; Zachariae, E. D.; Scavenius, C.; Kløverpris, S.; Oxvig, C.; Petersen, S. V.; Enghild, J. J.; Sørensen, E. S. Transglutaminase 2-catalyzed intramolecular cross-linking of osteopontin. *Biochemistry* **2016**, *55* (2), 294−303.

(33) Giachelli, C. M.; Steitz, S. Osteopontin: a versatile regulator of inflammation and biomineralization. *Matrix Biol.* **2000**, *19* (7), 615−622.

(34) Dowd, T. L.; Rosen, J. F.; Li, L.; Gundberg, C. M. The Three-Dimensional Structure of Bovine Calcium Ion-Bound Osteocalcin Using 1H NMR Spectroscopy. *Biochemistry* **2003**, *42* (25), 7769−7779.

(35) Gupta, H. S.; Wagermaier, W.; Zickler, G. A.; Raz-Ben Aroush, D.; Funari, S. S.; Roschger, P.; Wagner, H. D.; Fratzl, P. Nanoscale Deformation Mechanisms in Bone. *Nano Lett.* **2005**, *5* (10), 2108−2111.

(36) Poundarik, A. A.; Diab, T.; Sroga, G. E.; Ural, A.; Boskey, A. L.; Gundberg, C. M.; Vashishth, D. Dilatational band formation in bone. *Proc. Natl. Acad. Sci. U. S. A.* **2012**, *109* (47), 19178−19183.

(37) Ural, A.; Vashishth, D. Hierarchical perspective of bone toughness − from molecules to fracture. *Int. Mater. Rev.* **2014**, *59* (5), 245−263.

(38) Thurner, P. J.; Chen, C. G.; Ionova-Martin, S.; Sun, L.; Harman, A.; Porter, A.; Ager, J. W., Iii; Ritchie, R. O.; Alliston, T. Osteopontin deficiency increases bone fragility but preserves bone mass. *Bone* **2010**, *46* (6), 1564−1573.

(39) Duvall, C. L.; Taylor, W. R.; Weiss, D.; Wojtowicz, A. M.; Guldberg, R. E. Impaired Angiogenesis, Early Callus Formation, and Late Stage Remodeling in Fracture Healing of Osteopontin-Deficient Mice. *J. Bone Miner. Res.* **2007**, *22* (2), 286−297.

(40) Ducy, P.; Desbois, C.; Boyce, B.; Pinero, G.; Story, B.; Dunstan, C.; Smith, E.; Bonadio, J.; Goldstein, S.; Gundberg, C.; Bradley, A.; Karsenty, G. Increased bone formation in osteocalcin-deficient mice. *Nature* **1996**, *382* (6590), 448−452.

(41) Morsali, R.; Dai, Z.; Wang, Y.; Qian, D.; Minary-Jolandan, M. Deformation Mechanisms of""" ""Two-Part""" Natural Adhesive in Bone Interfibrillar Nano-Interfaces. *ACS Biomater. Sci. Eng.* **2019**, *5* (11), 5916−5924.

(42) Tai, K.; Ulm, F.-J.; Ortiz, C. Nanogranular Origins of the Strength of Bone. *Nano Lett.* **2006**, *6* (11), 2520−2525.

(43) Lai, Z. B.; Wang, M.; Yan, C.; Oloyede, A. Molecular dynamics simulation of mechanical behavior of osteopontin-hydroxyapatite interfaces. *J. Mech. Behav. Biomed. Mater.* **2014**, *36*, 12−20.

(44) Gao, C.; Peng, S.; Feng, P.; Shuai, C. Bone biomaterials and interactions with stem cells. *Bone Res.* **2017**, *5*, 17059.

(45) Vollrath, F.; Knight, D. P. Liquid crystalline spinning of spider silk. *Nature* **2001**, *410* (6828), 541.

(46) Naraghi, M.; Filleter, T.; Moravsky, A.; Locascio, M.; Loutfy, R. O.; Espinosa, H. D. A multiscale study of high performance double-walled nanotube- polymer fibers. *ACS Nano* **2010**, *4* (11), 6463−6476.

(47) Sheng, L.; Wei, T.; Liang, Y.; Jiang, L.; Qu, L.; Fan, Z. Ultra-high toughness all graphene fibers derived from synergetic effect of interconnected graphene ribbons and graphene sheets. *Carbon* **2017**, *120*, 17−22.

(48) Papkov, D.; Zou, Y.; Andalib, M. N.; Goponenko, A.; Cheng, S. Z.; Dzenis, Y. A. Simultaneously strong and tough ultrafine continuous nanofibers. *ACS Nano* **2013**, *7* (4), 3324−3331.

(49) Motta, M.; Moisala, A.; Kinloch, I. A.; Windle, A. H. High performance fibres from ' ''dog bone'carbon nanotubes. *Adv. Mater.* **2007**, *19* (21), 3721−3726.

(50) Fantner, G. E.; Oroudjev, E.; Schitter, G.; Golde, L. S.; Thurner, P.; Finch, M. M.; Turner, P.; Gutsmann, T.; Morse, D. E.; Hansma, H. Sacrificial bonds and hidden length: unraveling molecular mesostructures in tough materials. *Biophys. J.* **2006**, *90* (4), 1411−1418.

(51) Thompson, J. B.; Hansma, H. G.; Hansma, P. K.; Plaxco, K. W. The backbone conformational entropy of protein folding: experimental measures from atomic force microscopy. *J. Mol. Biol.* **2002**, *322* (3), 645−652.

(52) Hansma, P. K.; Fantner, G. E.; Kindt, J. H.; Thurner, P. J.; Schitter, G.; Turner, P. J.; Udwin, S. F.; Finch, M. M. Sacrificial bonds in the interfibrillar matrix of bone. *J. Musculoskeletal Neuronal Interact.* **2005**, *5*, 313.

(53) Thorpe, C. T.; Birch, H. L.; Clegg, P. D.; Screen, H. R. C. The role of the non-collagenous matrix in tendon function. *Int. J. Exp. Pathol.* **2013**, *94* (4), 248−259.

(54) Chakraborty, P.; Zuckermann, R. N. Coarse-grained, foldable, physical model of the polypeptide chain. *Proc. Natl. Acad. Sci. U. S. A.* **2013**, *110* (33), 13368−13373.

(55) Frazao, C.; Simes, D. C.; Coelho, R.; Alves, D.; Williamson, M. K.; Price, P. A.; Cancela, M. L.; Carrondo, M. A. Structural evidence of a fourth Gla residue in fish osteocalcin: biological implications. *Biochemistry* **2005**, *44* (4), 1234−1242.

(56) Lin, T.-J. Force field parameters and atomistic surface models for hydroxyapatite and analysis of biomolecular adsorption at aqueous interfaces. Ph.D. Thesis, The University of Akron, 2013.

(57) Burger, C.; Zhou, H.-w.; Wang, H.; Sics, I.; Hsiao, B. S.; Chu, B.; Graham, L.; Glimcher, M. J. Lateral packing of mineral crystals in bone collagen fibrils. *Biophys. J.* **2008**, *95* (4), 1985−1992.

(58) Young, M. F. Bone matrix proteins: their function, regulation, and relationship to osteoporosis. *Osteoporosis Int.* **2003**, *14* (3), 35−42.